True to size surface mapping with neutral helium atoms

Sam M. Lambrick,[1, *] Adrià Salvador Palau,[2, †] Poul Erik Hansen,[3]
Gianangelo Bracco,[4] John Ellis,[1] Andrew P. Jardine,[1] and Bodil Holst[2]

[1] *Department of Physics, Cavendish Laboratory, JJ Thomson Avenue,*
University of Cambridge, Cambridge, CB3 0HE, UK
[2] *Department of Physics and Technology, University of Bergen, Allégaten 55, 5007 Bergen, Norway*
[3] *Danish Fundamental Metrology A/S Kogle Alle 5, 2970 Hørsholm, Denmark*
[4] *CNR-IMEM, Department of Physics, University of Genova, V Dodecaneso 33, 16146 Genova, Italy*
(Dated: April 15, 2021)

Three-dimensional mapping of microscopic surface structures is important in many applications of technology and research, including areas as diverse as microfluidics, MEMS and geoscience. However on the nanoscale, using established techniques for such imaging can be extremely challenging. Scanning helium microscopy (SHeM) is a new technique that uses neutral helium atoms as a probe, enabling completely non-destructive imaging. The technique is broadly applicable and ideal for many otherwise difficult to image materials such as insulators, ultra-thin nano-coatings and biological samples. Here we present a method for implementation and operation of a stereo helium microscope, by applying the photometric stereo method of surface reconstruction to helium microscopy. Four detectors around the sample are typically required, but we show how sample rotation can be used to perform stereo reconstruction with a single detector instrument, or to improve the quality of the reconstructed surface by increasing the number of independent measurements. We examine the quality of the reconstructed surface and show that for low aspect ratio good absolute height is recovered. For features with height/width ~ 1 the shape of the surface is still recovered well (8% error) despite multiple scattering and masking of the helium beam by surface topography. Therefore it is possible to perform accurate reconstruction of the shape of nanoscale structures with a height to width ratio of at least unity.

I. INTRODUCTION

Accurate measurements of surface topography are essential to many fields of modern research. However, applying established techniques on the micro- and nano-scale is often difficult; for example, electron microscopy is complicated by the local secondary electron emission properties of surfaces [1] and scanning probe methods are limited by the tip profile [2]. The emerging technique of scanning helium microscopy (SHeM) [3–5], which uses a beam of neutral atoms, provides a promising new opportunity. Thermal energy helium atoms have several advantages as imaging probes; they are inert and their energies are very low compared to other particle probes used for imaging, such as electrons or helium ions. Specifically, the energy of the atoms in a supersonic helium beam is approximately $50\,\mathrm{meV}$, corresponding to a de Broglie wavelength of around $0.05\,\mathrm{nm}$ [6]. These energies are between three and six orders of magnitude lower than the energies typically used in electron and helium ion imaging [7]. Furthermore, thermal helium atoms scatter from the outermost electron density distribution of the surface without any penetration into the material [6] and propagate in straight-line trajectories that are unaffected by electromagnetic fields. Thus helium atoms are capable of providing information about the true geometrical structure of a surface [6, 8]. Together, these properties mean

SHeM is ideal for probing the topography of samples that are difficult to measure otherwise, either because conventional probe-surface interactions limit the measurements, or because the sample can react or deteriorate during the process of imaging. In particular, helium is well suited to imaging insulators and biological samples, as well as ultra-thin coatings and other nano-materials that have a significant three dimensional structure.

3D structure determination has recently been reported using helium atoms [9] using the stereophotogrammetry technique, which was applied to taxonomic studies of the trichomes on a mouse eared cress leaf, and dorsal skin of a Port Jackson shark. The method works by triangulation; the sample was tilted by known angles and corresponding points on the surface were used to obtain a small number of 3D coordinates with a single-detector. The method is thus similar to observation using an optical stereomicroscope with a single source of illumination. The points used for triangulation were mapped manually between subsequent images; the difficulty being that each point in the image has to be carefully mapped to the corresponding point in each rotated image, and more importantly that several rotations about different axes are required to obtain a good three-dimensional reconstruction [10].

An alternative approach to 3d imaging with atoms has been made possible by the recent discovery that unlike highly prepared 'pristine' atomic surfaces, which scatter with an angular distribution containing strong specular and diffracted components [6, 8], many 'unprepared' technological surfaces scatter diffusely with an approximate cosine like distribution [11–14]. The cosine-like dis-

tribution appears and is centred on the surface normal, even when the sample is illuminated on a microscopic level. On a macroscopic scale, when averaging over a significant fraction of surface, such behaviour has long been known as Knudsen's cosine law [15–18]. However, identifying similar behaviour on a microscopic scale means that by sampling the scattered distribution in several different directions, the local surface orientation can in-principle be determined, and hence by integration the 3D surface profile. An exact cosine distribution does not even need to be assumed, providing sufficient independent angular measurements are obtained. In order to make use of this principle, the second generation of SHeM instrument that has been developed in Cambridge includes the capability to simultaneously acquire images from 4 detectors arranged around the incoming helium micro-probe.

In this article, we present a three-dimensional surface profile reconstruction technique which we refer to as 'heliometric stereo', an adaptation of the photometric stereo method to helium microscopy. Photometric stereo uses photographs of an object illuminated from different angles to reconstruct a 3D image of the object, by using differences in the light intensities due to the different angles of illumination [19]. Heliometric stereo works analogously, but, taking into account the differences of image formation, instead of changing the illumination angles, the observation angles are changed.

In photography or traditional light microscopy an object is illuminated with a number of light sources. An image of the object is produced by the light rays scattered from the object going through a series of lenses, and then being projected onto a light-sensitive detector/film with spatial resolution. In helium microscopy, and other scanning imaging techniques such as SEM, images are formed by illuminating the sample point by point with a focused or collimated beam and measuring the intensity collected by one or several detectors. By rastering the sample under the beam (equivalent to rastering the beam over the sample), an image viewed from the incident beam is generated through Helmholtz reciprocity; the same process that is used in scanning electron microscopes and in dual photography [20]. Fig. 1 shows the method of image production via scanning in comparison to image formation with broad illumination. In principle, helium microscopy could also use the same imaging principle as photography. However, it is not possible with present technology to build a helium detector with spatial resolution, though suggestions have been made that it could be done with field ionisation detection [21, 22].

The lateral resolution of SHeM images is determined by the size of the helium micro-probe incident on the sample, which in turn determines the minimum extent of each pixel in the image. The image contrast is governed by the angular size and position of the helium detectors, which sample the distribution of atoms scattered from the illuminated point on the surface. Practically, SHeM images are always limited by shot-noise, due to the finite flux of atoms. When using pinhole collimation to form
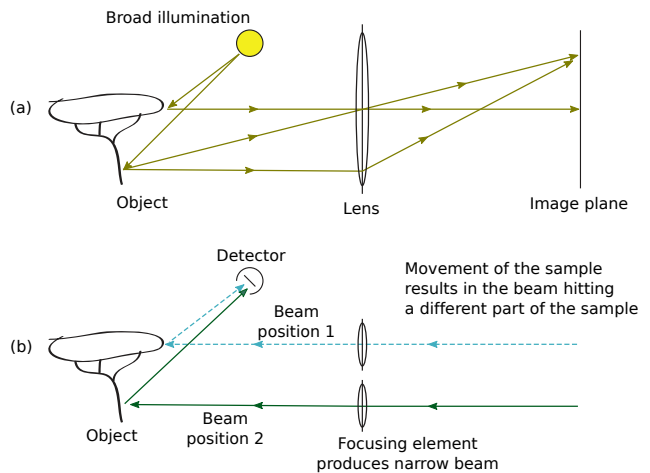

FIG. 1. (a) The process of image formation using a lens and broad illumination and (b) the alternative method of producing images by scanning a focused probe follows from inverting the direction of the light rays to give an image appearing as if it were formed behind the focusing element, in (b) the two beam positions would not happen simultaneously. Understanding the projection allows the right coordinate system to be used for heliometric stereo.

the microprobe the flux drops strongly with increasing resolution [23, 24]; consequently the smallest helium microprobe reported to date is 350 nm [4, 25, 26]. Fortunately, higher intensities can be achieved by focussing the beam with a Fresnel zone-plate; theoretical calculations [24, 27] have estimated that the helium microprobe can be reduced to a diameter of order 10nm.

In the design of a neutral helium microscope, it is important to distinguish between the lateral resolution, which is determined by the size of the helium beam and gives the ability to distinguish between features spatially separated on the sample, and the 'angular resolution' which is given by the solid angle covered by the detector opening. The smaller the solid angle, the more well defined the angle of detection is. Hence the 'angular resolution' determines the possibility of accurately knowing the intensity of scattered helium in a particular direction but does not have an impact on the minimum feature size observable. In order to achieve good angular resolution, detectors are designed to cover as small a solid angle as permitted by the signal to noise ratio of the instrument [28].

In the current work we show that photometric stereo applied to helium (heliometric stereo) is an ideal technique for 3D image reconstruction in helium microscopes, because the point-by-point illumination of the sample allows for a straightforward implementation of the reconstruction process. Only a few images are required for surface reconstruction, which is important as it typically takes much longer to acquire images in a SHeM instrument, compared to electron or He ion microscopy. Heliometric stereo requires detection at multiple angles, which

can be simultaneously achieved in a microscope with multiple helium detectors, but we also show how sample rotation can be used to obtain multiple independent intensity measurements in a single detector instrument. We discuss both normal and non-normal incidence helium beams; the latter which when combined with rotation allows reconstruction of otherwise inaccessible parts of the sample surface. Finally, we show how the quality of the reconstruction is affected by the presence of significant multiple scattering or regions of the surface which do not have direct line of sight to the helium source or detector.

The remainder of the paper is organised as follows. Section II begins with an overview of the photometric stereo method, which is then developed to establish heliometric stereo, and ends with an example 3D reconstruction. Then follows a discussion of possible extensions and additional considerations (section III). Results are presented on image reconstruction on two technological relevant shapes: a sample with modest topology, which is simulated with a microscope set up corresponding to existing SHeM instrumentation, and a sample with high aspect ratio. The former is used to examine the effects of SNR and the number of detectors while the latter is used to examine the role of multiple scattering and the limits of the technique (section IV). The paper finishes with a discussion of factors to consider when designing a helium microscope for use with heliometric stereo and an outlook for the technique (section V).

II. GENERAL METHOD: HELIOMETRIC STEREO

A. The photometric stereo technique

The established technique of photometric stereo relies on the assumption that a point on the surface of the image will scatter light with a given angular distribution, known as a bidirectional reflection distribution function (BRDF), which gives the scattered intensity as a function of the incoming and outgoing angles [29]. If the camera position is fixed, the intensities recorded in the camera will depend only on the local surface orientation and the scattering distribution; and for the same material and surface condition, all points on the sample can be assumed to have the same scattering distribution.

If the bidirectional scattering distribution function is known, a series of images obtained by illuminating the sample from a different directions can be used as intensity maps to infer the local surface orientation, and thus the local surface gradient. These gradients may then be integrated over the surface to give a 3D height map of the sample.

1. Obtaining the surface normals

Photometric stereo techniques generally assume Lambertian scattering, a type of scattering that corresponds to a surface which is a perfect diffuse light scatterer [19]. Lambertian scattering is also referred to as cosine scattering, as the light intensity values recorded at pixel (x', y') in the camera image is

$$I_{(x',y')} = \rho \cos \theta = \rho \, \hat{\boldsymbol{n}} \cdot \hat{\boldsymbol{d}}, \tag{1}$$

as illustrated in in Fig. 2 (a) for scattering from position (x, y) on the surface. In the current work we use (x, y) to refer to a spatial position in a coordinate system we are interested (could be arbitrary but usually that of the sample with the z axis parallel to the overall sample normal) while (x', y') refers to a position in the image. Here, θ is the angle between the surface normal and the incident light source, $\hat{\boldsymbol{n}}$ is the unit normal to the surface, $\hat{\boldsymbol{d}}$ is a unit vector from the surface to the light source, and ρ is the albedo or reflectance factor for that point on the surface. For light the outgoing angle, χ, does not appear in the intensity equation as the $\cos \chi$ dependence in the scattering is exactly compensated by the $(\cos \chi)^{-1}$ dependence from the projection of the surface area into the camera. Instead, the cosine term arises from the projection of the light source onto a surface at angle θ; the area of surface that the light hits is proportional to $(1/\cos \theta)^{-1}$.

Where there are multiple light sources we can write

$$\vec{I}_{(x',y')} = \rho \mathsf{D} \hat{\boldsymbol{n}}, \tag{2}$$

in which $\vec{I}$ is a m-dimensional vector of pixel intensities corresponding to m images taken from those different light sources. D is a $m \times 3$ matrix containing the normalized vectors connecting the light sources and the point (x', y') for each image. As there are three degrees of freedom in the system there have to be at least three non co-planar vectors in D for a unique solution to exist, corresponding to three distinct light sources. The surface normals, $\hat{\boldsymbol{n}}$, and reflectances, ρ, can be obtained from eq. (2) by solving the system of linear equations for each pixel in the image,

$$\rho_{(x',y')} = |\mathsf{D}^{-1} \vec{I}_{(x',y')}|, \tag{3}$$

$$\hat{\boldsymbol{n}}_{(x',y')} = \frac{1}{\rho} \mathsf{D}^{-1} \vec{I}_{(x',y')}. \tag{4}$$

If the height of the surface can be described by a function of the lateral position, i.e. $z = f(x, y)$, then

$$\hat{\boldsymbol{n}}(x, y) = \boldsymbol{\nabla} F(x, y, z) = \boldsymbol{\nabla}[z - f(x, y)]. \tag{5}$$

Thus once the surface normals are found, the gradient field given by eq. (5) may be integrated to obtain an equation of the surface, i.e. a topographic map of the sample.
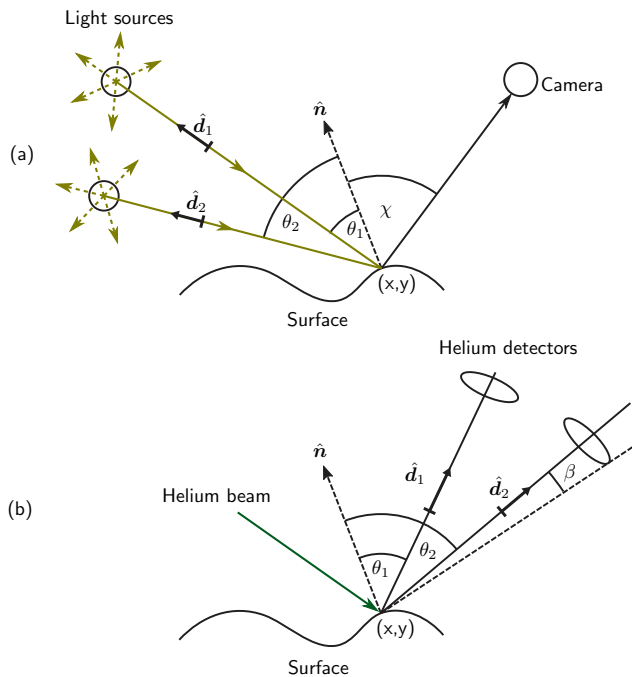
FIG. 2. Correspondence between photometric stereo, (a), and heliometric stereo, (b). $\hat{\boldsymbol{n}}$ is the local unit normal to the surface, $\hat{\boldsymbol{d}}_i$ are the directions to the light sources or detectors. In the case of photography multiple light sources are used to generate images with different $\hat{\boldsymbol{d}}$ vectors, in the case of helium microscopy multiple detectors are used with a single focused illumination to give different $\hat{\boldsymbol{d}}$ by the reciprocity of focused beam imaging.

2. Surface reconstruction from normals

The gradient field in eq. (5), can be integrated using established methods from the field of surface reconstruction. Here, we use Harker and O'Leary's MATLAB toolbox [30]. For a more detailed explanation and mathematical proofs their work should be referred to [31, 32] as only a brief outline is given below.

A least squares approach is used to find the matrix of heights Z that upon derivation with respect to x and y gives the least distance from the measured gradient field, given by the normals $\hat{\boldsymbol{n}}$. The discrete derivatives of Z can be written as $\mathsf{L}_x\mathsf{Z}$ and $\mathsf{Z}\mathsf{L}_y^\mathsf{T}$. The matrices $\hat{\mathsf{Z}}_x$ and $\hat{\mathsf{Z}}_y$ represent the *measured* gradient field given by $\hat{\mathsf{Z}}_x = n_x/n_z$, $\hat{\mathsf{Z}}_y = n_y/n_z$. Thus, the least squares minimization corresponds to minimizing ϵ:

$$\epsilon = \left\| \hat{\mathsf{Z}}_x - \mathsf{Z}\mathsf{L}_x^\mathsf{T} \right\|_F^2 + \left\| \hat{\mathsf{Z}}_y - \mathsf{L}_y\mathsf{Z} \right\|_F^2, \qquad (6)$$

where $\|...\|_F$ represents the appropriate norm. Expanding and differentiating to minimize ϵ yields an equation with a unique solution [31].

3. Image projection

A complication of the photometric stereo technique is the way a physical object is projected onto an imaging plane so that pixel indices can be related to physical coordinates. In a camera (without the use of a telecentric lens) a perspective projection is formed, meaning that displacements on the image do not correspond directly to physical distances: the physical distance between two pixels changes across the image depending on the distance to the object and the focal length of the lens used. Helium microscopes, however, are pixel-by-pixel imaging instruments that necessarily produce images in an orthographic projection: the image is formed through the two-dimensional rastering of the sample by fixed distances between pixels. Thus there is a fixed correspondence between pixel locations in an image and physical locations on the sample.

In either photography or helium microscopy the sample is mapped onto a plane with a projection. In a photograph the object is projected through the lens onto the camera sensor, the axis of projection is then normal to the camera. The projection axis corresponds to the z axis in eqs. (1-5). Translating to helium microscopy the z axis in the heliometric stereo method is parallel to the beam and the points x', y' used in the method are defined by the direction of the beam, and not necessarily in the plane of the motion of the microscope's nanopositioning stages. The implications of the projection have to be considered carefully when sample rotations are used to acquire extra 3D information on the sample (see Section III).

4. Applying photometric stereo to helium microscopy

We are in the fortunate situation that cosine distributed scattering can also be used to model the scattering of neutral helium atoms from many surfaces, where it is known as Knudsen's cosine law [18]. Although helium scattering from highly prepared 'pristine' atomic surfaces shows complex scattering distributions [6, 8], many 'normal', 'unprepared' or 'technological' surfaces studied to date are consistent with an approximate cosine distribution [15–18] and recent SHeM image modelling shows excellent agreement with simulations that use a cosine model of scattering [12–14]. Under Knudsen's scattering law, the photometric stereo method may therefore be applied to helium microscopy and in fact requires very little modification. The scattering geometry is illustrated in Fig. 2(b), where each point on the sample is assumed to scatter with a cosine distribution about the local surface normal $\hat{\boldsymbol{n}}(x, y)$. (Deviations from a perfectly cosine distribution are mitigated by over-constraining the system, as discussed below.)

Assuming cosine scattering of helium atoms from the sample surface, the scattered intensity into an element of

solid angle $d\Omega$ is

$$dI_{(x',y')} \propto \cos\theta \, d\Omega, \qquad (7)$$

where θ is the angle between the detector and the surface normal at the point (x,y). The intensity reaching a particular detector is then

$$I_{(x',y')} \propto \int_{\Omega_D} \cos\theta \, d\Omega, \qquad (8)$$

where Ω_D is the solid angle of the detector entrance aperture. In certain existing helium microscopes the detector apertures occupy a significant fraction of solid angle, covering a wide range of detection angles [4] so the extent of the solid angle needs to be considered. However, providing the aperture is not too large, as is usually the case [3], since the cosine function varies slowly, the integral can be approximated by $\Omega_D \cos\theta$. For an aperture occupying a small circular region of the solid angle hemisphere ($\lesssim \%$ of the total hemisphere), with half-cone angle β and angle from the surface to the center of the aperture of θ, it can be shown that the signal becomes (see appendix A)

$$I_{(x',y')} \propto \frac{1}{2}\pi \cos\theta \, (1 - \cos 2\beta), \qquad (9)$$

which also has a cosine dependency with θ. Thus, where detector apertures are small or occupy circular regions of equal solid angle then the intensity detected in a helium microscope can be written as

$$I_{(x',y')} \propto \cos\theta = \rho \, \hat{\boldsymbol{n}} \cdot \hat{\boldsymbol{d}} \qquad (10)$$

which is the equivalent to eq. (1). The application of the basic photometric stereo method in helium microscopes follows with $\hat{\boldsymbol{d}}$ defined as the unit vector from the point (x,y) to the detector.

If, due to the practical considerations of design, the solid angles of the detector apertures are not all equal, or if the detectors do not have the same efficiency the modification of eq. (2) is

$$\vec{I}_{(x',y')} = \rho\hat{\Omega}\mathsf{D}\hat{n}, \qquad (11)$$

where $\hat{\Omega}$ is a constant diagonal matrix containing the solid angles and detection probability of the various detectors and D and ρ have the same meaning as in eq. (2). In practice the values in $\hat{\Omega}$ can be attained via a calibration of the detectors prior to the acquisition of the data, or by numerically solving the equation provided that there exist enough independent observations.

B. Simulated helium images

We use simulated helium micrographs to test the heliometric stereo method. These micrographs are generated by ray-tracing, with each ray representing a helium atom [13, 14, 33]. The method assumes straight line trajectories of atoms within a 3D space consisting of the sample and local environment within the microscope. The rays are traced, scattering off the surfaces, until they either intersect a detector surface or leave the simulation region, with both directly scattered rays and multiply scattered rays included. All images used in the current work are generated using a cosine model of the scattering events.

In the first set up, we use instrument dimensions which have already been realised experimentally, to demonstrate what can be achieved with present technology. We use a simulated beam-source and detector geometry comparable to the one used in the existing SHeM in Cambridge [3]. As shown in Fig. 3, our set up assumes a helium beam diverging from a circular virtual source, corresponding to a the skimmer in the supersonic nozzle expansion. The helium microprobe is then formed by collimation using a pinhole of 2 μm diameter [34]. The 'virtual source' is assumed to be a uniformly emitting disc of radius 50 μm at a distance 50 cm behind the pinhole (*i.e.* rays are emitted from all elements of the surface and at all angles with the same probability). The large distance between the virtual source and pinhole, compared to the distance between pinhole and sample (1 mm), means that the beam has only a small divergence. Thus the spot size of the beam is approximately 2 μm, with a depth of field of several millimetres.

To obtain simulated images, four detectors were placed at 90° from each other and at 35° from the sample normal, with a normal incidence beam ($z = z'$), as shown in Fig. 3. Given these source and detection geometries, only the number of rays to use and the sample itself need to be provided to complete the simulation set up. The number of simulated rays were chosen to provide a realistic level of signal to noise (SNR) to recent experiments. The data from Fig. 1 in Lambrick et. al [12] was used as a representative experimental SHeM image. The darkest pixel in the image was assumed to be representative of the background signal and was subtracted, then the standard deviation and mean intensity from pixels on a flat region of the sample were taken to be the noise and the signal level respectively, giving an SNR of ~ 30. All simulated images used below have equal or lower signal to noise ratios than that experimentally measured value.

C. Heliometric reconstruction

In order to test the heliometric stereo technique, we use a test sample containing a series of technologically inspired geometric structures: an octagonal pyramid with a depressed top, a rectangular pyramid, a cap of a sphere, a series of increasingly deep pyramidal depressions and a three-dimensional triangle. The feature sizes are all in the 5-100 micron range and have low aspect ratios ($\sim 0.1 - 0.4$), with detailed dimensions given in Fig. 18 of the appendix. These geometries were chosen for different reasons: The increasingly deep pyramidal depres-
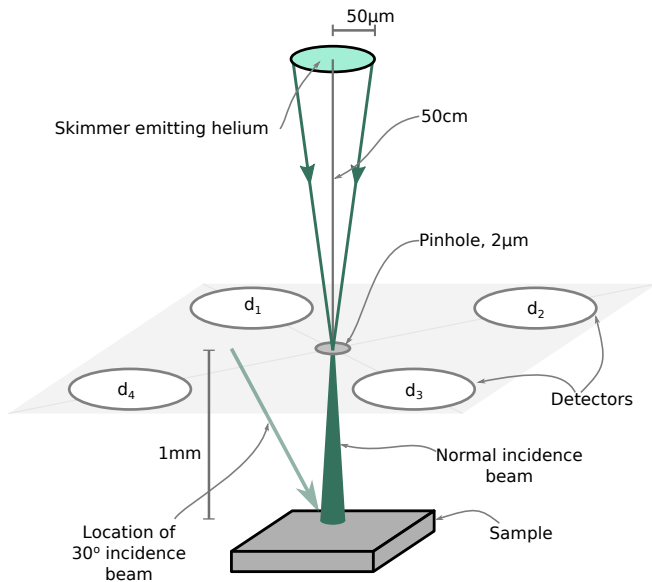
FIG. 3. The simulation set up that was used to generate the images of the test sample and the model of the source used. Four detectors were placed on a plane equidistant around the sample with an angle of $35°$ to the sample normal. The beam rays are generated in the virtual pinhole with a divergent distribution assuming a circular uniform virtual source shown at the top of the figure (skimmer), for the non-normal incidence simulations the beam source was moved but the detectors were kept the same locations.

sions tests of the quality of reconstruction with depth. The octagonal pyramid with a depressed top tests how the reconstruction handles complicated geometries with a a further depression. The rectangular pyramid has different slopes and is aimed to test the reconstruction precision with angle. The spherical cap is intended to test for the reconstruction of smooth geometries and continuously changing surface gradients. Finally, the three-dimensional triangle has vertical surfaces and tests reconstruction of geometries with abruptly varying heights. Due to their regular forms, these samples resemble artificial structures and we note that the sharp edges would make it very difficult to image them true to size using secondary electron emission based techniques.

Fig. 4 illustrates the stages of producing synthetic helium images from the known sample surface and using them to reconstruct the surface. 1. The original sample surface is input to the ray tracing simulations; 2. Four images are generated from the four detectors: it can be seen that the lightest areas in the images point towards the respective detector while the dark areas point away. 3. The four images are then used to calculate the surface normals, by solving equation 4, which represent the gradient field of the surface. 4. Finally, the gradient field is integrated to find a reconstructed surface. It can be seen that there is a good qualitative match between the original surface and the reconstructed surface in the

first and fourth panels. The quantitative accuracy of the reconstruction is discussed in section IV.

1. Accuracy of reconstruction

Fig. 6 shows a normalised percentage error plot of the basic reconstruction shown in Fig. 4, while figure 5 shows selected line profiles of the original and reconstructed surface. The error has been normalised by the height of the tallest feature on the surface: the large pyramid structure on the bottom left. The overall RMS error was 2.4%, however we note that there are sections of significantly larger error within the plot. It should be noted that the 2.4% RMS error will be a combination of an intrinsic error to the method and errors resulting from the noisy initial data (simulated images). Noise in the images will result in noise in the gradient field, which will relate in a non-trivial way to errors in the reconstruction. The impact of SNR is discussed further in the next section. Noticeable are the sharp edges on the central pyramid and the deepest of the trenches on the top left side of Fig. 4. Therefore we may say that reconstruction works well with two identified caveats, the first being surfaces that are parallel to the beam (vertical in the case of normal incidence) and hence do not get illuminated; and second multiple scattering: the deepest trench causes a significant amount of multiple scattering, which results in a loss of the well defined relationship between signal and surface orientation.

In the next section we consider how increasing the number of detectors through the use of rotations, and how varying the image SNR affects the accuracy of the reconstruction.

III. EXTENSIONS AND FURTHER CONSIDERATIONS

A. Non-cosine and multiple scattering

As discussed in Section II A 4 cosine scattering is a good first approximation for the scattering of helium atoms from technological samples. However, this type of scattering does not always fully explain experimental data. For example, the existence of non-topographic forms of contrast where the scattering distribution is not fixed across the sample breaking one of the assumptions of heliometric stereo [28, 35] necessarily require deviation from cosine scattering. Heliometric stereo can be extended to more general forms of scattering by emulating preexisting photometric stereo methodologies, for example by using a parameterized scattering distribution that is fitted to the data (see, for example, [36–38]). In the current work, the albedo or reflectance factor is assumed to be sufficient.

An additional contrast feature of helium atom microscopy is multiple scattering which is taken here to
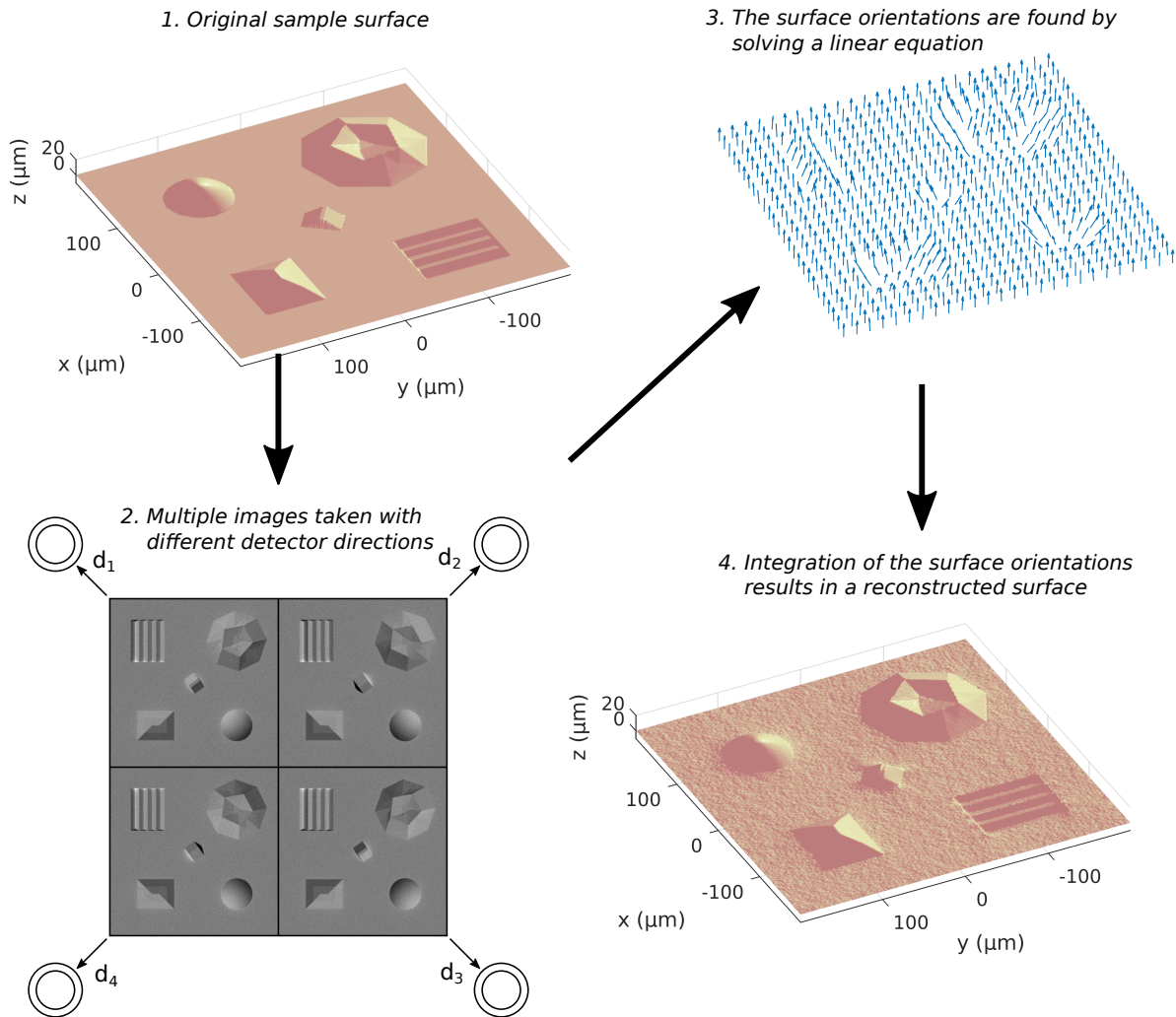
FIG. 4. Overview of the basic heliometric stereo method. 1. The original sample. 2. The sample is imaged using multiple detectors placed in different directions to yield a series of helium images, in the example shown here, the set up shown in Fig. 3 was used to generate the simulated helium images. 3. Those helium images are used as the terms $\vec{I}$ in equation 4 to acquire the surface normals. 4. Finally, as the normals to a surface are the gradient of that surface they may be integrated to give a reconstructed surface. The accuracy of the reconstruction presented here is discussed in section II C.

mean the situation when the helium atoms are 'bouncing' from one distinct area on the sample to another [12, 13, 26]. This can cause regions in images to appear brighter, in particular where there is significant topography in the form of deep or tall features (high aspect ratios). In the present work it is assumed that overconstraining the problem combined with the albedo factor can largely negate the issue of multiple scattering for samples with modest topography. The implications of multiple scattering are considered further in section IV D.

B. Masked regions

A significant contrast feature of helium microscopy is the presence of masking [13, 14, 26], where the direct line of sight between the beam-sample intersection and the detector is blocked by another part of the sample. Qualitatively, masks can be thought of as similar to conventional shadows (they are notably different in mechanism however, shadows are a lack of illumination rather than a lack of detection). As the line of sight is blocked, the detected signal has no bearing on the normal of the surface.

While 3D information is coded in the size and shape of the masks, directly including masked areas in the reconstruction of the normals leads to substantial error. Where the images contain significant masking the sim-
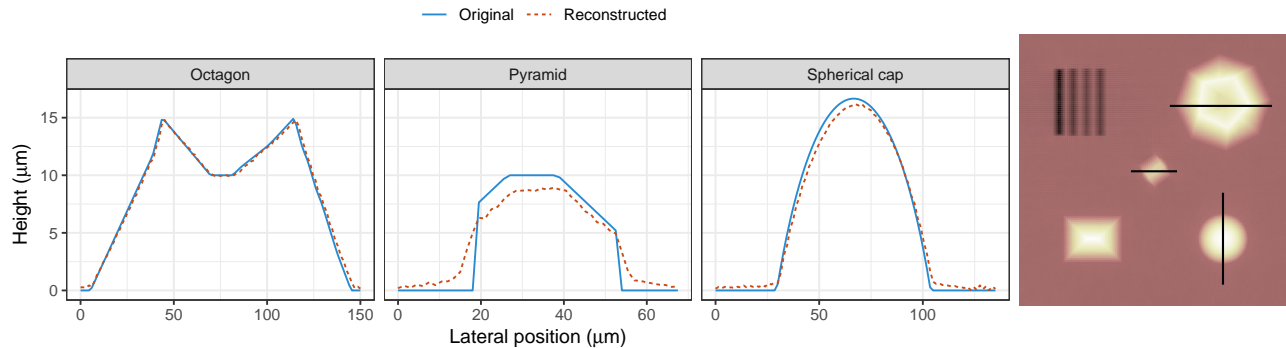
FIG. 5. Three lines profiles extracted from the reconstructions presented in figure 4. The location of the line profiles are shown on the height map of the original surface on the far right. The high quality of the reconstruction in the case of the octagonal and spherical cap features is evident, while the limitations near sharp edges can be seen in the case of the pyramidal feature.
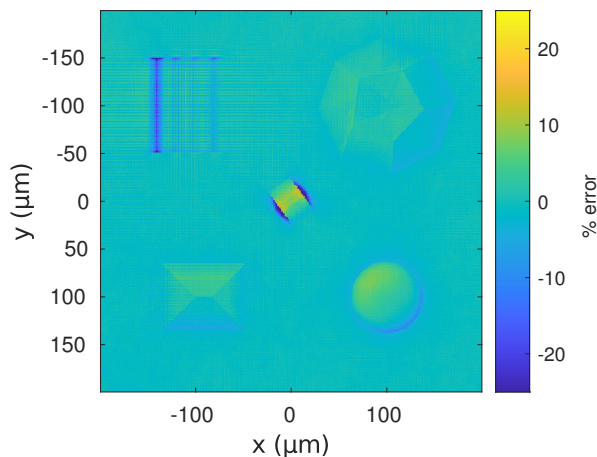

FIG. 6. The percentage error between the reconstructed surface using the 4 detector geometry shown in Fig. 3 and the original surface (surface plots of both are shown in Fig. 4). The error has been normalised by the height of the tallest of the large pyramid structure on the bottom left of the sample. The RMS percentage error was 2.4% overall.

plest approach is to exclude the masked regions, however care must be taken not to underconstrain parts of the reconstruction. If only a small fraction of the image is masked ($\sim 1 - 5\%$ of an image) it is possible that they need not be excluded—the low intensity recorded in the masks would render the normal to be perpendicular to the detection direction, not a bad approximation where the regions concerned are small.

In the current work, masking is addressed using an automatic threshold method: masked regions of images are excluded from the reconstruction by choosing an intensity level below which pixels are discarded. The upper bound that the threshold can be is obtained by imposing that for every point in the image the following system of equations has at least three independent linear equations:

$$W\vec{I}_{(x',y')} = W\rho\hat{\Omega}\mathrm{D}\boldsymbol{n}. \qquad (12)$$

The masking threshold is chosen as a scalar smaller than the threshold value that visually captures the masking contributions, which can be seen in the intensity histogram of the images as peaks in small intensity values (see Appendix D).

An alternative to the threshold approach, a weighting strategy is possible in order to handle masked regions, or regions with low signal to noise ratio. For example, one can weight regions with lower intensities less so that when a value of $I_{(x',y')}$ is fed into the linear least squares minimisation algorithm used to solve eq. (11), that value contributes less [39]. A straightforward way to achieve a weighting would be to make the weighting of pixels to monotonically increase with the intensity. Note that in Poisson statistics the standard deviation of the count rate is inversely proportional to its square root (higher intensities mean that the quality of the signal is better [40]).

C. Sample rotation

Helium microscopes generally have a poor signal to noise ratio compared to modern photography which poses a problem when reconstructing 3D surfaces, as the data quality is lower than in the case of photography. Fortunately, we can obtain more independent observations of each point and improve the quality of the reconstruction by rotating the sample. The same 'trick' can also be used to allow helium microscopes that do not possess enough physical detectors to perform heliometric stereo. If the rotation is performed about the beam axis, for example azimuthal rotation of a sample with a normally incident beam, there is a straight-forward mathematical implementation of eq. (11) as the image plane, and hence coordinate system are the same throughout all images. If the sample is rotated about a different vector, the correspondence between points on rotated images becomes more complex, although there can be benefits of doing so.
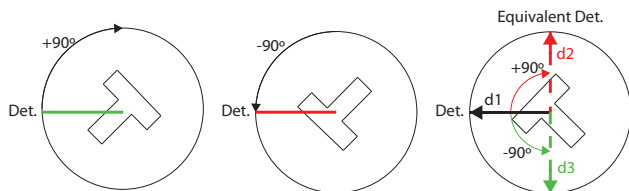
FIG. 7. Rotation in heliometric stereo. After collecting the first image (right) the sample is rotated by $90°$ and two further images are obtained (middle and left), these images may be rotated to lie ontop of the original image if the reverse rotations are applied to the detector vectors $\hat{d}_2$ and $\hat{d}_2$ as shown in the right panel.

1. Rotation about the beam axis

As helium microscopy produces images in an orthographic projection, rotating the sample about the beam axis mathematically corresponds to an inverse rotation of the detector position (see Fig. 7). By rotating the new images I so that each (x', y') coordinate in the image corresponds to the (x', y') coordinates of the rest of the images, the new data can be incorporated as an additional detector. Additionally, the corresponding vector $\vec{d}$ has to be rotated in the opposite direction to the sample by the same angle (see the equivalent detectors in Fig. 7).

Aligning two images of the same sample at different rotation angles can be done through image recognition software, or through a rotation of the scanning pattern. Image recognition software sometimes requires human input, which can lead to error in the reconstruction. Alternatively, rotating the scanning pattern with the sample so that each pixel of the image always corresponds to the same position on the sample produces images aligned down to the accuracy of the positioning stage. The latter method is chosen in this paper to remove human error from the results.

Applying rotations about the beam axis allows for i) the implementation of heliometric stereo with a single detector, and ii) a convenient method to obtain more data and reduce reconstruction error.

2. Rotation about other axes

For rotation about an axis other than the beam axis, the beam hits different regions of the sample at different angles, so that there is no complete bijective correspondence (no one-to-one correspondence) between the points of two images (see Fig. 8). On one hand, this makes it difficult to use sample rotation to get more independent data points for eq. (4). On the other hand, rotations about axes other than the beam axis allows to image parts of the sample that otherwise would never intersect the incident beam as a result of shadowing.
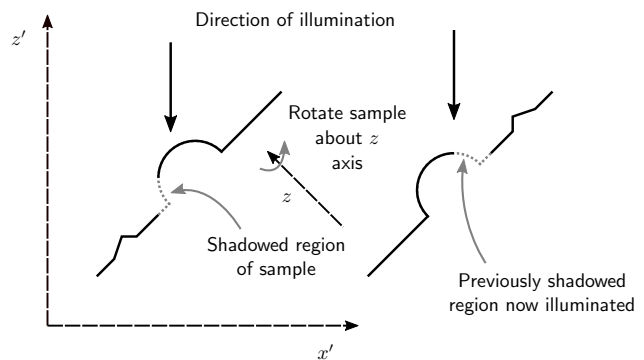

FIG. 8. Sketch of the lack of bijective correspondence between helium microscopy images in the case of rotation not about the beam axis. Regions of the sample that are shadowed can be imaged if we rotate about an axis other than the beam axis. The primed coordinates are the heliometric stereo coordinates with the z' axis parallel to the beam while the unprimed coordinates are those of the sample with z parallel to the overall sample normal.

The fact that shadowing prevents the beam from intersecting all sample points in every rotated image is not an impediment to recovering the 3D surface of a sample from a set of images taken at different rotation angles. To do so, several different sample surface reconstructions can be combined into a single surface after the application of heliometric stereo. Such an approach contrasts with rotating the sample about the beam axis, in which eq. (7) is over-determined.

IV. DETAILED RESULTS

A. Rotation to give more detectors

As discussed in section III C 1, rotations about the beam axis can provide a greater number of effective detectors beyond the number of physical detectors. A simulation was performed with the same detector set up as described in Fig. 3, but with the sample rotated about the beam axis in intervals of $72°$ to give a total of 5 sets of 4 images. Reconstructions were then performed using different levels of signal to noise and different numbers of rotations (and hence effective detectors).

Fig. 9 gives the root mean square error for different combinations of detectors and rotations for three different levels of signal to noise. It is noted that a similar improvement to the reconstruction is obtained both with an improvement of a factor of 2 in SNR or with an increase of the number of images by a factor 4. Since the noise in neutral helium microscopy is dominated by shot noise [41], both improvements require the same increase in acquisition time. There also seems to be a minimum level of error which is not improved by adding more information. That error is likely a result of failures of the
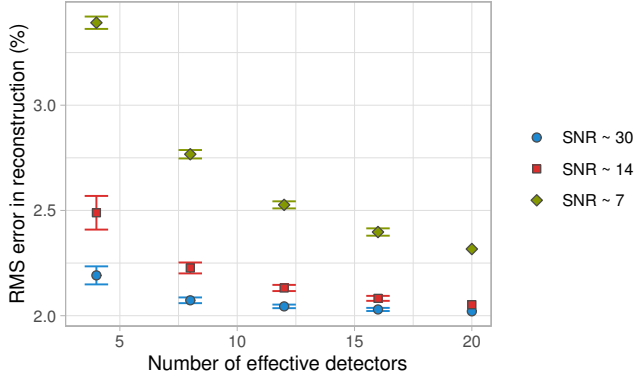
FIG. 9. The root mean squared error (RMS) for the reconstructed surfaces as a function of the number of effective detectors for three different levels of signal to noise ratio (SNR) in the simulated images. The error bars represent the standard deviation of the errors for the reconstructions: using different combinations of the rotations. The RMS error tends towards a lower limit of $\sim 2\%$. The limit on the overall RMS error is due to elements of the sample that heliometric stereo cannot recover well with the cosine model, i.e. the sharp walls on the side of the central feature and the deepest trench on the top left feature (in the error map in Fig. 4). It can be noted that improvements in SNR ratio have a similar impact as increasing the number of detectors by an equivalent amount: SNR improvement by a factor of 2 (and thus measuring time by ~ 4) has a similar impact as increasing the number of detectors by 4.

method near vertical surfaces (such as around the central feature) or deep features that have a higher proportion of multiple scattering (such as the top left feature on the error map in Fig. 4). Reducing the number of detectors to 3 can result in good reconstructions, but can also cause the reconstruction to fail (if detectors 1, 2, & 3 are taken from Fig. 4 for example), demonstrating the importance of slightly overconstraining the problem to get reliable results.

B. Using a single detector

As discussed above heliometric stereo can also be applied to a microscope with only a single detector provided rotations about the beam axis can be performed. It must be note the all areas of a surface need to be covered by at least 3 and preferably 4 images and that due to the use of matrix-based techniques to reconstruct the surface from the gradient field rectangular images need to be used. This can be addressed either by i) padding the images with the downside of some parts of the sample being unconstrained, or ii) using a special scanning pattern rotated counter to the sample rotation. The latter approach is taken here.

Single-detector heliometric stereo was successfully tested using the images obtained by rotating the sample but only using the first detector, effectively creating a
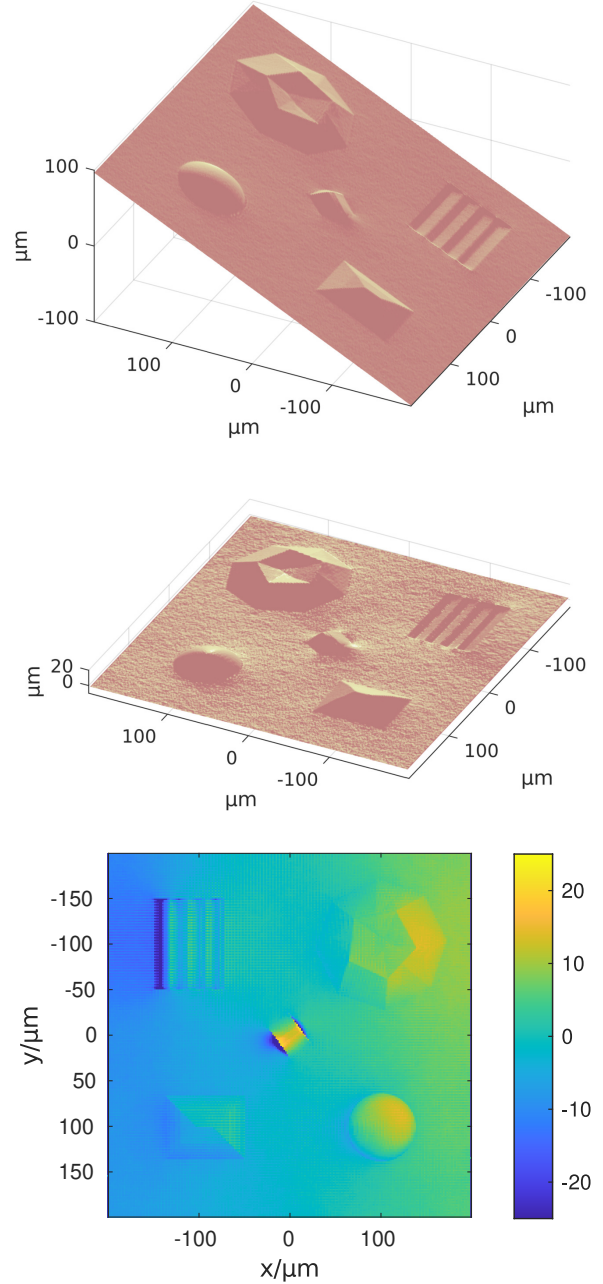

FIG. 10. For non-normal incidence the initial reconstruction is tilted due to the sample being 'viewed from an angle' (top) but may be rotated (middle) and then compared to the original surface. The root mean squared error (bottom) was 16.7%, the higher calculated error compared to the normal incidence case is due to a slight overall tilt, $\sim 0.4°$ left on the sample after rotation which can be seen in the error image on the left. Correcting for the $\sim 0.4°$ overall tilt by rotating the surface yeilds an overall RMS error of 3.4%, slightly greater but comparable to the error found in the normal incidence case.

reconstruction from 5 images with only a single detector. The images used for the reconstruction and the recon-

structed surface are shown in Fig. 20 in the appendix. The method of rotating the scanning pattern along with the sample can be seen in the simulated helium images there. The possibility of implementing heliometric stereo using a single detector is important because the current generation of helium microscopes operate in this configuration.

C. Non-normal incidence

As described in Section II, it is possible to reconstruct the height of a sample using a beam that is incident the sample at an angle. In general, the incidence direction of the beam defines the z axis of the reconstruction method, and thus the scanning pattern used by the sample manipulation in the microscope should take this into account.

Once the surface is reconstructed it will appear tilted, as the helium images are taken 'from an angle'. The surface can then be rotated to match the original sample. To demonstrate the process, heliometric stereo has been applied to simulated images with an incidence angle of 30° and the results are shown in Fig. 10.

Non-normal incidence can be combined with sample rotation as described in Section III C 2: multiple reconstructions are combined rather than using the additional images to over-constrain a single reconstruction. An advantage of using rotations in this manner is that parts of the sample that are not illuminated in one sample orientation are illuminated in another. Fig. 11 compares the errors in the reconstructed surface for i) non-normal incidence and rotations with ii) a single non-normal incidence data-set and iii) a normal incidence data set. The reconstruction from a set of 4 images with a single sample orientation manages to capture a vertical surface in the central feature on the sample better than the normal incidence reconstructions (due to the surface not being parallel to the beam in the non-normal case).

However as can be seen in the averaged image simply averaging the 5 sets of data does not produce a better reconstruction than the normal incidence case (effectively adding more detectors), thus a more complex averaging mechanism is needed. A form of weighted averaging could be employed, however it will not be simple to identify which reconstructions to give a high/low weight.

D. The impact of aspect ratio on reconstruction

The test sample considered in the previous section demonstrates the ability of the method to reconstruct surfaces with relatively low aspect ratios where there is little masking or multiple scattering. In order to understand how the method works with higher aspect ratios and where masking and multiple scattering start to affect the reconstruction accuracy, a simple sample was designed with 4 rods whose height and slope were varied. Fig. 12 shows an example with an aspect ratio of 0.6.
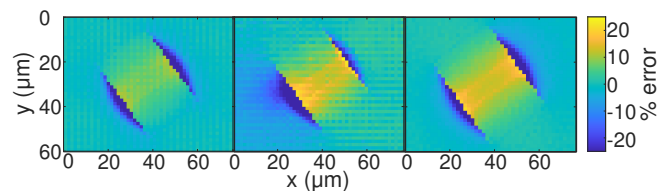

FIG. 11. The errors in the reconstructed surface for: normal incidence and rotations (left), a non-normal incidence set of images without rotations (middle), and non-normal incidence with rotations (right). Note that the single orientation non-normal incidence reconstruction captures well one vertical surface and the other very poorly, the high error region being 1-2 pixel rather than 3 pixels wide—the beam intersected the right-hand side of the sample here. However, when all the different orientations are averaged in a simple manner the reconstruction loses the sharp verticals: non-normal incidence rotations do give us more accurate information, but simple averaging does not fully make use of them.

The aspect ratio was quantified as the height over half the separation between the centres of two rods. For the simulated images used in this section the same virtual microscope set up was used as presented in Fig. 3.

Fig. 13 shows how the accuracy of the reconstructed height of the rods, measured as the difference between the height in the circular regions on the top and the four corners of the reconstruction, varies with the aspect ratio. To evaluate what proportion of the error was being introduced as a result of multiple scattering, reconstructions were also performed with only the single scattering contribution of the images as a comparison. Presented are the height accuracy both with and without multiple scattering and with and without applying thresholding. We note that the error introduced by multiple scattering is present at all but the smallest aspect ratios, red points, but remains less than 20% for aspect ratios less than 0.5. Using only single scattering, blue points, the reconstruction keeps a high accuracy until masking becomes a significant feature in the images. The application of thresholding does not appear to increase the accuracy of the reconstructed height, green points, though there is an effect on the shape as discussed in the next paragraph; however thresholding does improve the accuracy at high aspect ratios for the reconstruction where multiple scattering is excluded, purple points. It is notable that even where the multiple scattering is significant and is causing a quantitative error in the reconstructed the qualitative shape of the reconstructed surface is still recovered well, as can be seen in Fig. 12, which is for 'rods' of aspect ratio 0.6.

Observing Fig. 12 we note that while under conditions where the height is not reconstructed to a high accuracy, it does appear that the shape of the surface is still reconstructed well. In order to quantify the accuracy of the shape reconstruction we allow the reconstructed surface heights to vary: $z_2 = \alpha z + \beta$ and perform a least squares minimisation to find α, β that fit the original surface best.
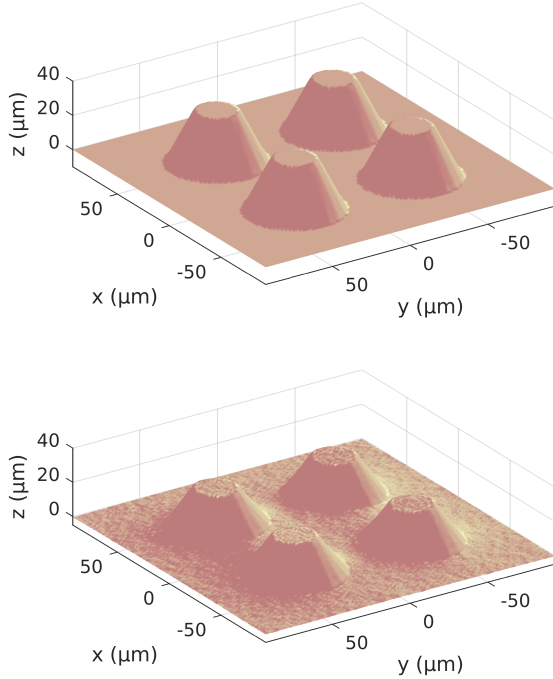
FIG. 12. The original surface with and aspect ratio of 0.6 and the reconstruction with the microscope set-up shown in Fig. 3. It can be seen that there is a good qualitative reconstruction despite the height only being reconstructed as 75% of the original height. The other samples used in the aspect ratio investigation have same footprint and cone top but with varying slopes of the sides.
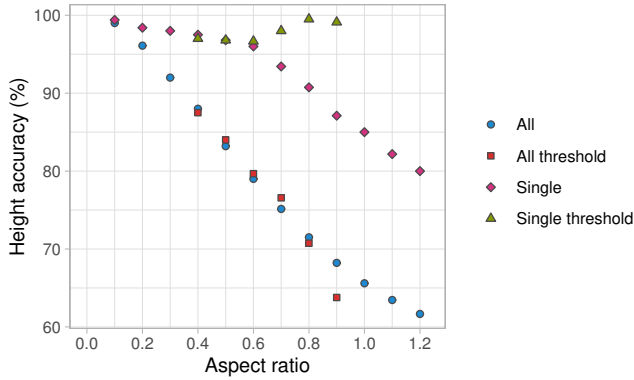

FIG. 13. Accuracy of the reconstructed height with respect to the aspect ratio of the sample. 100% represents the original height. Reconstructions were performed with and without multiple scattering (red and light blue), and with the thresholding method for removing masking introduced in Sec. III B (green for multiple scattering and the threshold method and purple for single scattering). The error bars represent the level of noise in the regions of reconstruction.
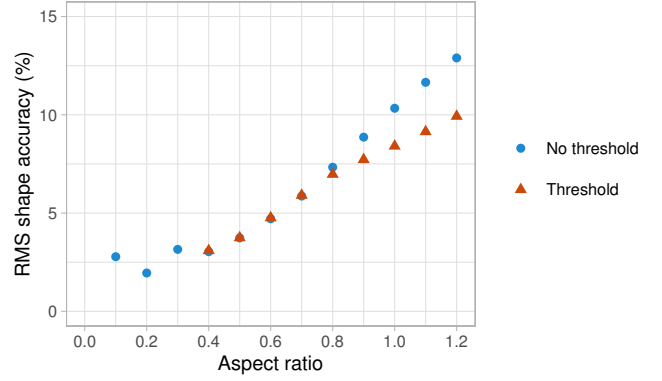

FIG. 14. RMS error between the original surface and the scaled reconstruction normalised relative to the height of the original sample. To consider the accuracy of the method in reconstructing the *shape* of the surface, the reconstructed surface is allowed to scale linearly to best fit the original surface. It can be seen that the errors remain below 10% for aspect ratios below 1 and below 5% for aspect ratio < 0.7. It can also be seen quantitatively that the application of thresholding to remove masked regions of the sample improves the accuracy of the shape reconstruction.

The RMS error is then calculated for the scaled surface and normalised by the height of the cone structure. The results are shown in Fig. 14, where we note that the overall accuracy in the shape of the reconstruction remains better than 10% for all the samples below aspect ratio 1 and that for aspect ratios < 0.7 the RMS error is less than 5%. Overall there is good reproduction of the shape of the surface for low to modest aspect ratios in the sample. It is also shown that the application of the thresholding method discussed in section III B improves the accuracy of the shape reconstruction where there is masking present. An example showing where the thresholding method improves the shape of the reconstructed surface is in Fig. 15 with the aspect ratio 0.8 sample. Here, without thresholding, masking distorts the footprint of the cone, but removing that masking from the reconstruction restores the footprint accurately.

E. The near future: high resolution, high aspect ratio features

The 3D imaging of samples with high aspect ratio features on the nanoscale presents a significant challenge to current technology. We note from the results in the previous section that good shape reproduction is found with the aspect ratio 1 sample, to about 8% error. Its height is reconstructed as 66% of the original height. Thus high aspect ratio features are reconstructed well qualitatively with the current formalism. However, multiple scattering limits the quantitative accuracy of the height, which represents the main obstacle to the application of the method to high aspect ratio features.
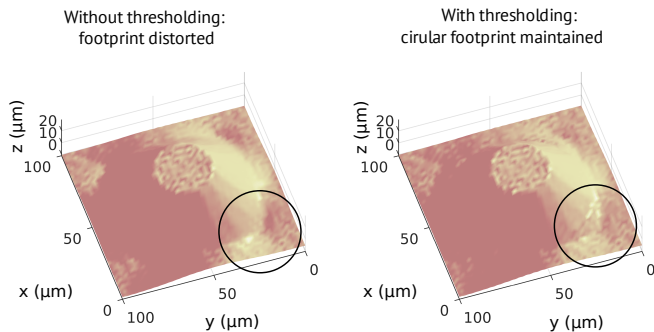
FIG. 15. The reconstructed surfaces with and without thresholding applied for the aspect ratio 0.8 sample. It can be seen that the circular footprint of the cone is distorted where the thresholding is not applied and thus masked regions are included in the reconstruction. By removing the masked regions, the circular footprint is restored (see black circle).

Due to the scale independent nature of the ray tracing simulation we may consider the interesting possibility of applying heliometric stereo to a helium microscope with the estimated best possible resolution of 10 nm [27]. At such resolutions reconstruction of samples with heights of ~ 100 nm should be possible. A simulation was performed with the appropriate scale between beam width and rod height, it was chosen to change from the sample normal to the detectors from $35.3°$, as in Fig. 3, to an angle of $19.5°$ in order to reduce any masking from the simulated images. A shape error of 7% was found and a height 60% of the original height was reconstructed. It is noted that the change of detector positions to minimise masking has slightly improved the shape reconstruction but made the absolute height error worse due to an increased detection of the multiple scattering signal.

V. DISCUSSION

A. Design recommendations

There are certain design principles that that should be considered when designing a neutral helium microscope that is intended to perform heliometric stereo reconstruction. These considerations are given below and while some of them are necessary for the application of heliometric stereo to be possible, it should be noted that some may also be counter to other scientific or practical considerations.

First, in order to perform heliometric stereo without rotating the sample then at least 4 not co-planar detectors are needed. If 4 physical detectors are not possible then the ability to rotate the sample about the beam axis is required, which is likely to be easier with a normal incidence microscope, and in that case at least 2 detectors are recommended so that only one rotation is needed per

reconstruction. More than 4 detectors may have benefits for difficult samples by allowing more aggressive thresholding and may allow the application of more advanced adaptations to heliometric stereo, but they are not necessary.

If at least 4 detectors are present then a non-normal incidence microscope would be more flexible as it allows the sample to be imaged from different directions, giving more 3D information. It would also allow detection on the specular condition that may be desirable in other helium scattering experiments. The detectors should, as close as possible, occupy circular regions of solid angle to maintain the cosine assumption, and the solid angle of the detectors should be kept modest, as far as the signal level allows, in order to reduce the possibility of 'partial masking' where only part of the detector is within line of sight of the sample. In order to keep the amount of masking modest we suggest that detectors should be placed not-too-far from the incidence direction to keep the amount of masking modest: we suggest no greater than $30 - 40°$. All the above requirements are already met by the 2nd generation SHeM being developed in Cambridge.

An alternative, potentially ideal, design of a helium microscope may involve detectors that can be rotated around the sample instead of fixed detector positions. Such a configuration would have a high degree of flexibility for both heliometric stereo and other experiments. However, such an instrument would be a major technical challenge that so far has not been demonstrated experimentally.

For a single detector microscope to perform reconstructions it is necessary to include the ability to rotate the sample about the beam axis to obtain a vector of intensities $\vec{I}$ (see Fig. 20), which must be the key consideration if designing a microscope for heliometric stereo without multiple detectors. In practice enabling such rotations will likely mean designing a machine for normal incidence or one that can be adapted to operate at normal incidence.

B. Constraints

There are two notable constraints on the application of heliometric stereo. The most important, which applies to all scanning helium microscopes, is the difficulty in obtaining an adequate SNR in the underlying measurements, given the incident helium intensity and the limited efficiency of neutral helium detectors. The finite SNR, together with the effect of multiple scattering, degrades the quality of the images and therefore the quality the subsequent 3D reconstruction. However, a high level of robustness to noise has been demonstrated in section IV B; specifically, reconstruction is successful with SNR levels well below those in recently published SHeM images. In addition, by rotating the sample to acquire a greater number of virtual detectors, the effective SNR can be further improved, albeit at the expense of longer

measurement durations.

A less fundamental limitation on the presented method is the reliance on the diffuse scattering assumption. Although diffuse scattering is the predominant mode for neutral helium atoms scattering from technological samples, other scattering distributions are also to be expected, although such deviations are likely to be highly sample specific, making general comments difficult. However, it is possible to distinguish between cases where the scattering distribution remains constant across the sample, and where it varies with position. If the scattering distribution is expected to be constant but not diffuse, Eqs (1), (2) and their dependencies must be re-written as it cannot be generally expressed as a matrix multiplication. Assuming a known distribution or distribution family, one can still numerically solve for $\hat{n}$ and the distribution parameters using well-established methods [36–38]. If the distribution family (its parametric expression) is not known, a non-parametric solver can be used, provided that there is enough experimental data [42]. Note that here the problem is to first find the function f so that $I = f(\hat{n}, \hat{d})$ where $\hat{d}$ is known point-by-point and I is measured and then invert it. If the parametric distribution varies across the sample, the problem is still solvable but doing so is significantly harder as the regions must be established in which there is a distribution shift. Fortunately, such problems have already been addressed in light scattering using the technique of orientation-consistency, which requires the measurement of sections with known orientations and similar scattering distributions [36]. Similar techniques could be potentially implemented for helium, especially in the case of samples with known ordered regions or structures.

C. Outlook

We note that diffraction at the detector opening (i.e. airy disk diffraction for a circular entrance aperture) will not influence the lateral resolution of the microscope. This is because the wavelength of the helium atoms for all practical purposes will always be less than 0.1 nm (the wavelength of a liquid nitrogen cooled beam). Thus, the beam spread introduced through diffraction at the detector opening is negligible even for nm lateral resolution[4, 25, 26]

Masking and multiple scattering were highlighted as issues with heliometric stereo, however, it has been shown that where they are only present in small parts of a set of helium images the overall reconstruction is still good. The thresholding method has been shown to improve the reconstruction results by removing masked regions of the sample from the reconstruction where there is sufficient constraint of the linear problem. Cases of large amounts of masking and significant regions of multiple scattering will occur where higher aspect ratios are present in the sample and new methods will need to be applied to acquire accurate reconstructions. Given the ability of the

ray tracing framework to model multiple scattering an iterative approach may be suggested as a route of further work where the initial reconstruction is simulated with ray tracing and the multiple scattering signal then removed from the original images. It may also be possible to combine heliometric stereo with triangulation-based photogrammetry where accurate heights of high aspect ratio features are needed.

We note that adaptations of photometric stereo could be also potentially be applied to stereo electron or stereo helium ion microscopes and that a considerable amount of work has already been done on stereo electron microscopy using techniques based around photogrammetry[43]. However, the challenge for the application of photometric stereo here is that for images generated by secondary electron imaging, the signal is strongly dependent on the geometry of the system - i.e. the signal is much stronger at edges, etc, - and, in general, there isn't a well defined angular selection of the detection. This makes true to size surface mapping difficult [1]. Some work has been done also on 3D helium ion microscopy imaging [44]. The problem with the secondary electron signal is similar here. For both stereo scanning electron microscopy and stereo helium ion microscopy the work done so far has relied on very many images being available for reconstructing the sample. In cases where beam damage is induced on the sample, the method presented here may be of particular interest.

VI. CONCLUSION

We present an adaptation of photometric stereo to neutral helium microscopy: heliometric stereo. The method takes advantage of the dependency of the scattered intensity of a helium beam on the local normals of the sample. Through ray-tracing simulations of a comparable helium microscope with a spot size of 2 micron, we show that the heliometric stereo method is able to resolve the three-dimensional surface of microscopic samples by using just a few images. The reconstructed surface displayed a root mean squared error of roughly 2% of the characteristic length scale of the sample with a signal to noise ratio of just 30 in the images used. We find good shape reconstruction with samples with aspect ratio up to 0.6, with the shape being recovered with less than 5% error. Up to aspect ratio 1.2 with the error is less than 10%. The success at recovering the shape of the sample, even at high aspect ratios, raises the possibility of accurate high resolution and high aspect ratio 3D reconstructions in the near future.

The only condition for the implementation of heliometric stereo is that sufficient images of the sample are obtained to resolve the equations of the normals. For simple geometries this can be done with just three images, that can be obtained in a single experiment in a multi-detector helium microscope, or by rotating the sample three times. The easiness of implementation means that existing he-

lium microscope configurations can be adapted, for example by rotating the sample holders so that the helium beam is normally incident.

Heliometric stereo is a convenient method for three-dimensional resolution of helium microscopy samples, as the slow acquisition times of helium microscopes and the difficulty of manual point selection and tracing make other methods, like triangulation-based photogrammetry, more cumbersome to implement.

SUPPORTING DATA

A supporting data pack is provided to accompany this publication: `doi:10.17863/CAM.65551`.

ACKNOWLEDGEMENTS

Appendix A: Integration of aperture

In the simple model of diffuse contrast the detected signal, I, is a function of the angle between the surface normal and the centre of the detector aperture, ψ, and the half cone angle of the aperture, β. An integral is performed over the aperture modified by a cosine term, $\cos \chi$, where the angle χ is the angle between the surface normal and a single point on the aperture. Fig. 16 demonstrates the geometry of the model and the *signal* is thus

$$I \propto \int \cos \chi \, d\Omega. \tag{A1}$$

Defining θ to be the angle to the axis from the surface point to the centre of the detector aperture and φ to be the azimuthal angle around that axis the integral becomes

$$I(\psi, \beta) \propto 2 \int_0^\pi d\varphi \int_0^\beta d\theta \, \sin \theta \, \cos \chi. \tag{A2}$$

The cosine term, $\cos \chi$, may be written as the dot product between the unit normal to the surface and the normalised vector from the surface to the infinitesimal point on the aperture being summed. Defining φ to be relative to the x axis the unit normal is

$$\hat{\boldsymbol{n}} = \begin{pmatrix} \sin \psi \\ 0 \\ \cos \psi \end{pmatrix} \tag{A3}$$

which is fixed as ψ is a constant. the normalised vector from the surface to a point on the aperture, $\hat{\boldsymbol{d}}$ can be found by considering a Cartesian coordinate system on the model. The aperture lies on the unit sphere directly above the surface along the z axis by a distance $\cos \beta$. Referring to Fig. 17 points on the plane of the aperture have positions given by the 2D polar coordinates of $(r = z \tan \theta, \varphi)$, thus the components of the vector are $x = z \tan \theta \cos \varphi$, $y = z \tan \theta \sin \varphi$. Thus the normalised vector to the infinitesimal point on the aperture is

$$\hat{\boldsymbol{d}} = \frac{\cos \beta}{\cos \beta \sqrt{(1 + \tan^2 \theta \cos^2 \phi + \tan^2 \theta \sin^2 \varphi)}} \begin{pmatrix} \tan \theta \cos \varphi \\ \tan \theta \sin \varphi \\ \cos \beta \end{pmatrix} \tag{A4}$$

$$= \cos\theta \begin{pmatrix} \tan \theta \cos \varphi \\ \tan \theta \sin \varphi \\ 1 \end{pmatrix}. \tag{A5}$$

and the dot product is then

$$\cos \chi = \hat{\boldsymbol{n}} \cdot \hat{\boldsymbol{d}} = \cos \theta \, (\sin \psi \, \tan \theta \, \cos \varphi + \cos \psi) \tag{A6}$$
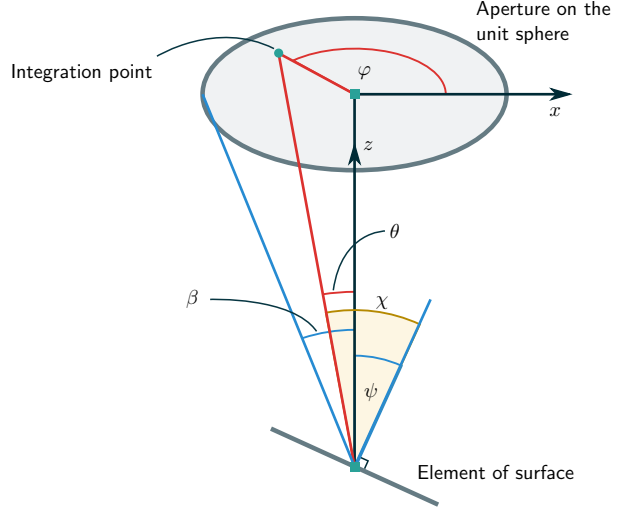

FIG. 16. The geometric set up of the contrast model. A circular aperture is on a unit sphere with an element of surface in the centre. The element of surface is at some angle ψ to the centre of the aperture and the extent of the aperture is defined by its half cone angle β. To calculate the signal intensity for a particular (ψ, β) half of the aperture is integrated over (by symmetry the intensity from the other half will be equal) through the angles (θ, φ). The integration variables and geometry are shown in red, and the variables of signal are shown in blue. The angle χ, in yellow, is between the normal to the surface element and the line from the surface element to the integration point, $\cos\chi$ weights the integral according to the cosine model of diffuse scattering.

which allows the signal, from eq. (A2), to be written as

$$I(\psi, \beta) \propto 2 \int_0^\pi d\varphi \int_0^\beta d\theta \, \sin \theta \, \cos \theta \, (\sin \psi \, \tan \theta \, \cos \varphi + \cos \psi). \tag{A7}$$

1. Analytic form

The integral in eq. (A7) can be evaluated analytically to give an explicit expression for the signal:

$$I \propto 2 \sin \psi \int_0^\pi \cos \varphi \, d\varphi \int_0^\beta \sin \theta \, \cos \theta \, \tan \theta \, d\theta$$
$$+ 2\pi \cos \psi \int_0^\beta \sin \theta \, \cos \theta \, d\theta \tag{A8}$$

$$= 0 + 2\pi \cos \psi \int_0^\beta \frac{1}{2} \sin 2\theta \, d\theta \tag{A9}$$

$$= \frac{1}{2} \pi \cos \psi \, (1 - \cos 2\beta). \tag{A10}$$

The above holds, however, only for a limited range of the (ψ, β) space—as the aperture gets larger and the angle
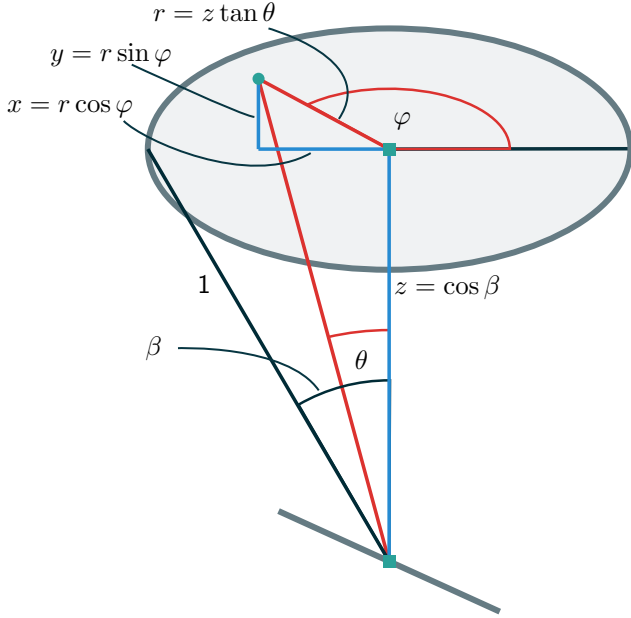
FIG. 17. The geometry deriving the vector to the infinitesimal point on the aperture via a Cartesian system. The three components of the vector from the surface element to an integration point on the detector aperture are shown in blue, x and y in terms of the intermediate variable r. As in Fig. 16 the integration variables are shown in red. Due to the symmetry of the system in the y axis the values of $-y$ and y are equivalent.

of the surface gets larger part of the aperture is going to fall 'behind' the surface, thus would contribution 0 to the integral. Eq. (A10) may thus be applied when

$$\psi + \beta \leq \frac{\pi}{2}. \tag{A11}$$

When eq. (A11) does not hold the cosine approximation of macroscopic apertures does not hold. Where detector apertures are small (small β this can largely be ignored.

Appendix B: Least squares reconstruction

The appropriate norm used in the least squares Reconstruction is the Frobenius norm on a matrix, which may be defined as

$$\|A\|_F = \sqrt{\text{tr}(AA^\mathsf{T})}. \tag{B1}$$

Appendix C: Sample dimensions

Fig. 18 details all the relevant sample dimensions. The dimensions have been rounded to the third decimal. A full reconstruction and source code with the complete measures are included in the supplementary documentation.
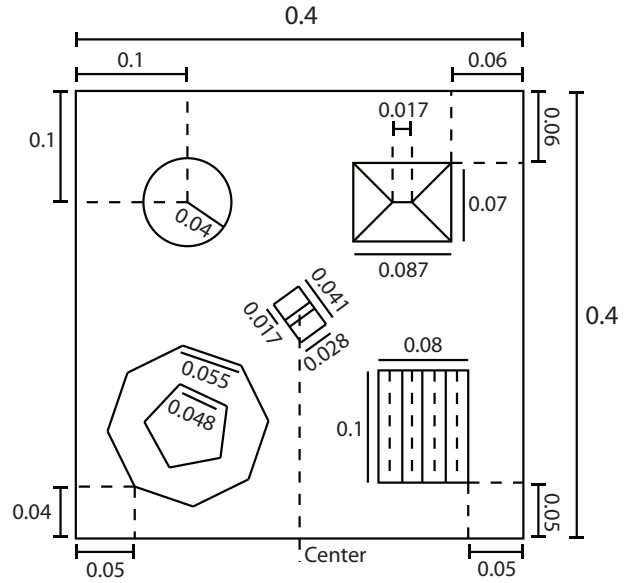

FIG. 18. Sample dimensions in µm. Note how the sphere protruding from the sample is only one third of a sphere of diameter 100 µm and therefore the measure shown is just its projection over the sample plane. The heights of each structure are: 16 µm for the sphere, 16 µm for the top right structure, -5 µm ,-4 µm, -5 µm, -8 µm from left to right for the four depressed structures at the bottom right of the sample, 15 µm for the pentagon at the bottom left and 10 µm for the central structure. Complete dimensions and code to generate the sample are included in the supplementary documentation.
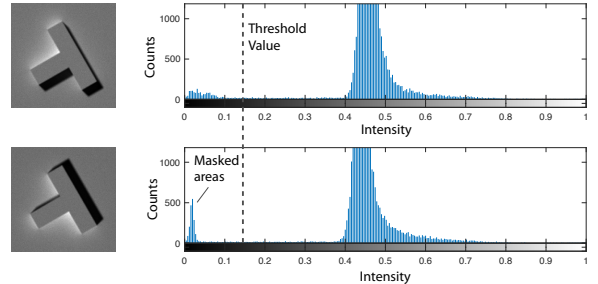

FIG. 19. Selection of uninformative masked regions by using the histogram of helium microscopy images.

Appendix D: Histogram-based threshold method

In order to select a masking threshold, a scalar is chosen so that it visually captures all masking contributions, while still ensuring that the reconstruction is fully determined at all points. These contributions can be seen in the intensity histogram of the images as peaks in small intensity values (see Fig. 19).
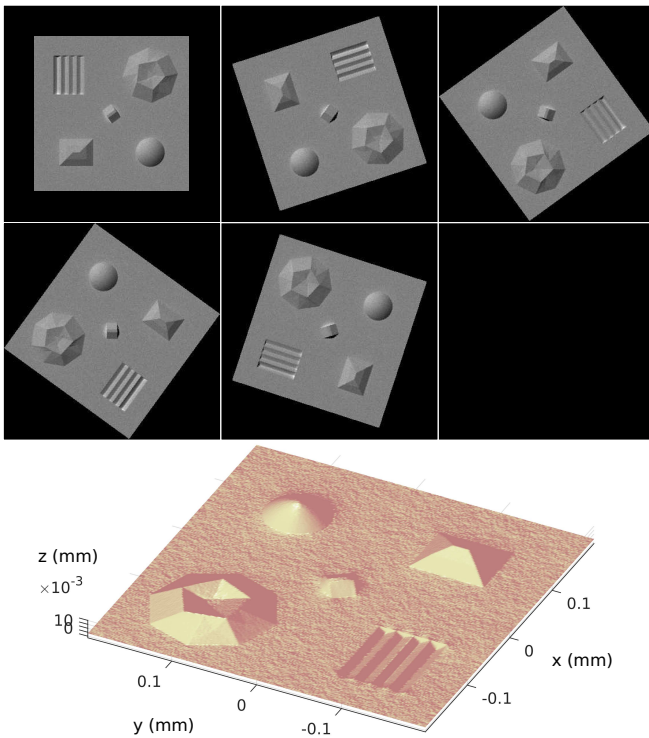
FIG. 20. 5 images taken with a single detector while rotating the sample—note the masks face in the same direction across the images indicating the detector direction. The scanning pattern was rotated along with the images to minimise under-constrained parts of the sample (parts that have fewer than 3 data points), thus the same region of the sample is imaged in each case.

Figure 20 shows 5 images taken with a single fixed position detector while rotating the sample and the scanning pattern. Note the masks maintain their orientation while the sample topography rotates. The scanning pattern is modified such that the same area of sample is observed in each image.

[1] M. T. Postek and A. E. Vladár, Scanning **35**, 355 (2013).
[2] J. Shen, D. Zhang, F.-H. Zhang, and Y. Gan, Applied Surface Science **422**, 482 (2017).
[3] M. Barr, A. Fahy, A. Jardine, J. Ellis, D. Ward, D. Ma-cLaren, W. Allison, and P. Dastoor, Nuclear Instruments and Methods in Physics Research Section B: Beam Inter-actions with Materials and Atoms **340**, 76 (2014).
[4] P. Witham and E. Sanchez, Review of Scientific Instru-ments **82**, 103705 (2011).
[5] M. Koch, S. Rehbein, G. Schmahl, T. Reisinger, G. Bracco, W. E. Ernst, and B. Holst, J. Microsc. **229**, 1 (2008).
[6] B.Holst and G.Bracco, "Surface Science Techniques," (Springer, 2013) Chap. 12, pp. 333–367.
[7] D. Joy, R. Ramachandra, and B. Griffin, Microscopy and Microanalysis **15** (2009), 10.1017/S1431927609092757.
[8] D. Farias and K.-H. Rieder, Rep. Prog. Phys. **61**, 1575 (1998).
[9] T. A. Myles, S. D. Eder, M. G. Barr, A. Fahy, J. Martens, , and P. C. Dastoor, Scientific Reports **9**, 2148 (2019).
[10] L. C. Gontard, R. Schierholz, S. Yu, J. Cintas, and R. E. Dunin-Borkowski, Ultramicroscopy **169**, 80 (2016).
[11] S. Lambrick et al., to be published.

[12] S. M. Lambrick, L. Vozdecky, M. Bergin, J. E. Halpin, D. A. MacLaren, P. C. Dastoor, S. A. Przyborski, A. P. Jardine, and D. J. Ward, Applied Physics Letters **116**, 061601 (2020).
[13] S. M. Lambrick, M. Bergin, A. P. Jardine, and D. J. Ward, Micron **113**, 61 (2018).
[14] A. Fahy, S. D. Eder, M. Barr, J. Martens, T. A. Myles, and P. C. Dastoor, Ultramicroscopy **192**, 7 (2018).
[15] M. Knudsen, *The kinetic theory of gases: some modern aspects*, 3rd ed. (London, London, 1950).
[16] D. R. O'Keefe and R. L. Palmer, Journal of Vacuum Sci-ence and Technology **8**, 27 (1971).
[17] F. Celestini and F. Mortessagne, Physical Review E **77**, 021202 (2008).
[18] R. Feres and G. Yablonsky, Chemical Engineering Science **59**, 1541 (2004).
[19] R. J. Woodham, Optical Engineering **19**, 191139 (1980).
[20] J.-J. Greffet and M. Nieto-Vesperinas, JOSA A **15**, 2735 (1998).
[21] D. J. Riley, M. Mann, D. A. MacLaren, P. C. Dastoor, W. Allison, K. B. Teo, G. A. Amaratunga, and W. Milne, Nano Letters **3**, 1455 (2003).
[22] R. Doak, Y. Ekinci, B. Holst, J. Toennies, T. Al-Kassab, and A. Heinrich, Review of scientific instruments **75**, 405

(2004).

[23] A. S. Palau, G. Bracco, and B. Holst, Physical Review A **94** (2016), 10.1103/PhysRevA.94.063624.

[24] M. Bergin, D. Ward, J. Ellis, and A. Jardine, Ultramicroscopy **207**, 112833 (2019).

[25] S. D. Eder, T. Reisinger, M. M. Greve, G. Bracco, and B. Holst, New. J. Phys. **14**, 73014 (2012).

[26] P. Witham and E. Sanchez, Crystal Research and Technology **49**, 690 (2014).

[27] A. Salvador Palau, G. Bracco, and B. Holst, Phys. Rev. A **95**, 13611 (2017).

[28] M. Barr, A. Fahy, J. Martens, A. P. Jardine, D. J. Ward, J. Ellis, W. Allison, and P. C. Dastoor, Nature Communications **7**, 10189 (2016).

[29] J. C. Stover (Society of Photo-Optical Instrumentation Engineers, 2012).

[30] `https://uk.mathworks.com/matlabcentral/fileexchange/43149`.

[31] M. Harker and P. O'Leary, in *2008 IEEE Conference on Computer Vision and Pattern Recognition* (2008) pp. 1–7.

[32] M. Harker and P. O'Leary, Journal of Mathematical Imaging and Vision **51**, 46 (2015).

[33] S. Lambrick, "slambrick/SHeM-Ray-Tracing-Simulation: SHeM Ray Tracing Simulation," (2018).

[34] T. Reisinger, G. Bracco, S. Rehbein, G. Schmahl, W. E. Ernst, and B. Holst, J. Phys. Chem A **111**, 12620 (2007).

[35] M. Bergin, S. M. Lambrick, H. Sleath, D. J. Ward, J. Ellis, and A. P. Jardine, Scientific Reports **10**, 1 (2020).

[36] A. Hertzmann and S. M. Seitz, IEEE Transactions on Pattern Analysis and Machine Intelligence **27**, 1254 (2005).

[37] S. Ikehata, D. Wipf, Y. Matsushita, and K. Aizawa, in *2012 IEEE Conference on Computer Vision and Pattern Recognition* (IEEE, 2012) pp. 318–325.

[38] D. B. Goldman, B. Curless, A. Hertzmann, and S. M. Seitz, IEEE Transactions on Pattern Analysis and Machine Intelligence **32**, 1060 (2009).

[39] T. Strutz, *Data fitting and uncertainty: A practical introduction to weighted least squares and beyond* (Vieweg and Teubner, 2010).

[40] J. Garnaes, P.-E. Hansen, N. Agersnap, J. Holm, F. Borsetto, and A. Kühle, Applied optics **45**, 3201 (2006).

[41] M. Bergin, *Instrumentation and contrast mechanisms in scanning helium microscopy*, Ph.D. thesis, Fitzwilliam College, University of Cambridge (2018).

[42] S. Ikehata and K. Aizawa, in *Proceedings of the IEEE Conference on Computer Vision and Pattern Recognition* (2014) pp. 2179–2186.

[43] L. A. Jácome, G. Eggeler, and A. Dlouhy, Ultramicroscopy **122**, 48 (2012).

[44] F. Vollnhals and T. Wirtz, Analytical Chemistry **90**, 11989 (2018).